Space Sci Rev (2008) 141: 235–264
DOI 10.1007/s11214-008-9365-9

The THEMIS Fluxgate Magnetometer

H.U. Auster · K.H. Glassmeier · W. Magnes · O. Aydogar · W. Baumjohann · D. Constantinescu · D. Fischer · K.H. Fornacon · E. Georgescu · P. Harvey · O. Hillenmaier · R. Kroth · M. Ludlam · Y. Narita · R. Nakamura · K. Okrafka · F. Plaschke · I. Richter · H. Schwarzl · B. Stoll · A. Valavanoglou · M. Wiedemann

Received: 12 December 2007 / Accepted: 21 April 2008 / Published online: 16 May 2008

Abstract The THEMIS Fluxgate Magnetometer (FGM) measures the background magnetic field and its low frequency fluctuations (up to 64 Hz) in the near-Earth space. The FGM is capable of detecting variations of the magnetic field with amplitudes of 0.01 nT, and it is particularly designed to study abrupt reconfigurations of the Earth's magnetosphere during the substorm onset phase. The FGM uses an updated technology developed in Germany that digitizes the sensor signals directly and replaces the analog hardware by software. Use of the digital fluxgate technology results in lower mass of the instrument and improved robustness. The present paper gives a description of the FGM experimental design and the data products, the extended calibration tests made before spacecraft launch, and first results of its magnetic field measurements during the first half year in space. It is also shown that the FGM on board the five THEMIS spacecraft well meets and even exceeds the required conditions of the stability and the resolution for the magnetometer.

Keywords Plasma physics · Substorm · Fluxgate magnetometer · Calibration

---

H.U. Auster (✉) · K.H. Glassmeier · D. Constantinescu · K.H. Fornacon · Y. Narita · K. Okrafka · F. Plaschke · I. Richter · B. Stoll
Institut für Geophysik und extraterrestrische Physik der Technischen Universität Braunschweig, Mendelssohnstrasse 3, 38106 Braunschweig, Germany
e-mail: uli.auster@tu-bs.de

W. Magnes · O. Aydogar · W. Baumjohann · D. Fischer · R. Nakamura · A. Valavanoglou
Space Research Institute, Austrian Academy of Sciences, Schmiedlstrasse 6, 8042 Graz, Austria

O. Hillenmaier · R. Kroth · M. Wiedemann
Magson GmbH Berlin, Carl Scheele Strasse 14, 12489 Berlin, Germany

E. Georgescu
MPE Garching, Giessenbachstrasse, Postfach 1603, 85740 Garching, Germany

P. Harvey · M. Ludlam
SSL at UCB, 7 Gauss Way, Berkeley, CA 94720-7450, USA

H. Schwarzl
IGPP at UCLA, Los Angeles, CA 90095-1567, USA

1 Introduction

Magnetic fields are essential in characterizing different plasma regions in and around the Earth's magnetosphere. Accurate measurements of the magnetic field vector along the orbits of the Themis spacecraft (hereafter referred to as probes) is the objective of the FGM experiment. The Themis probes follow elliptical, equatorial orbits. In the transfer orbits (coast phase) the probes have a perigee of about 1 Earth radius (R_E) and an apogee of about 15 R_E. The apogees of the final orbits vary from 10 R_E for the inner to 30 R_E for the outer probe. Changes of the orbits from the costal to the final phase and the seasonal variation of the apogee due to the Earth's orbital motion provide for an opportunity make to perform measurements of the magnetic field at various conditions in space. The magnetometer is designed to cover measurements in the solar wind, magnetosheath, magnetotail, and outer magnetosphere up to the region dominated by the Earth's dipole field. To achieve this goal several technical challenges had to be solved.

Frequent crossing of the radiation belt requires a reasonable radiation tolerance of the electronics, the spacecraft spin imposes a condition on high precision of timing, and the necessity to use the magnetic field at perigee for attitude determination defines the maximum measurement range. Furthermore, measuring the magnetic field within the required precision instrument design, magnetic environmental conditions, and constraints due to limited spacecraft resources had to be balanced.

The instrument itself is based on the heritage of the participating magnetometer teams, dating back to the missions such as the German Helios mission in the seventieth and the Russian Phobos missions in the eighties. Experience from magnetometer experiments on more recent missions such as Freja (Zanetti et al. 1994), Equator-S (Fornacon et al. 1999), Cluster (Balogh et al. 2001), Cassini (Dougherty et al. 2004), Double Star (Carr et al. 2005), VenusExpress (Zhang et al. 2006), or Rosetta (Auster et al. 2007; Glassmeier et al. 2007a) largely contributed to the successful design, fabrication, and operation of the Themis magnetometers. The instruments actually operating are very similar to those currently in use on the European Space Agency's cometary mission Rosetta (Glassmeier et al. 2007b; Auster et al. 2007) and VenusExpress (Zhang et al. 2006). Capabilities of these instruments are tailored to the science objectives of the Themis mission.

FGM benefits from a close cooperation between several institutions lead by the Institute of Geophysics and extraterrestrial Physics (IGEP) group of the Technical University Braunschweig. The hardware was developed at IGEP (sensor) and Magson GmbH Berlin (electronics). The Space Research Institute of the Austrian Academy of Sciences (IWF) in Graz supported the instrument development. Part procurement, integration, and qualification as well as the development of the onboard software has been done by the Space Science Laboratory of the University of California at Berkeley (UCB). Tests and preflight calibrations were performed in Braunschweig, Berlin and Graz. IGEP, supported by the University of California at Los Angeles (UCLA) group, is responsible for the in-flight calibration. The software for ground data processing has been developed by UCB, UCLA and the Max-Planck-Institute for extraterrestrial Physics (MPE) in Garching. This large team stands for a high level of expertise and guarantees an efficient adaptation of the existing hardware, software and other tools to Themis specific requirements.

Two features are specific for the Themis magnetometer experiments: a single sensor on a 2 m boom and the compact integrated instrument concept (Harvey et al. 2008). Placing just one sensor on a 2 m short boom is a novelty compared to, for example, the Cluster mission where each spacecraft has two sensors mounted on a 5 m boom. Limitations due to magnetic environmental conditions, which depend on the boom length, the number of sensors, and the level of spacecraft magnetic contamination are to be expected. An extensive magnetic cleanliness program was necessary to limit spacecraft disturbances below 1 nT DC and 10 pT AC at the sensor position. With only one sensor, the possibility to detect and remove s/c disturbances by a difference analysis is not possible anymore. The magnetic cleanliness program had to ensure that interferences caused by magnetic materials or generated by onboard currents are below the threshold given by the scientific requirements. In Sect. 5.2 remaining interferences detected by FGM measurements during commissioning as well as the policy for its removal are discussed. A detailed report describing methods and results of the magnetic cleanliness program is given by Ludlam et al. (2008).

The other Themis specific feature is that the spacecraft have a compact integrated instrument concept. The electronics is part of an instrument package inside the common electronics box. Therefore EMC and integration constraints are more difficult to meet. The fluxgate experiment can not be seen as an autonomous experiment. It is not placed, as usually done for larger spacecraft, in a stand-alone electronics box with internal DC/DC converter, own processing capability and well defined EMC conditions. The FGM electronics share a standard board inside the common electronics box together with the Power Control Unit (PCU). The secondary voltages are provided by a central DC/DC converter. The processing capability was divided into an instrument related part integrated in the FGM FPGA (Field Programmable Gate Array circuit), and a higher level onboard software implemented in the Instrument Data Processing Unit (IDPU). The integrated design had two consequences: first, the EMC environment depends on the operation status of nearby boards, and second, all parameters which can be influenced by environmental conditions had to be verified during and after spacecraft integration. Test facilities, which guarantee measurements with the full precision were developed, to verify instrument parameters during the integration process. The test and calibration strategy is described in detail in Sect. 4.4, while Sect. 5.2 deals with conducted interferences.

2 Science Requirements

Themis is a multi-spacecraft mission allowing to separate spatial and temporal variations in the Earth magnetosphere. After the four-spacecraft Cluster mission it is the second mission of this kind. The prime objective is the study of the physical causes of substorm onsets in the magnetotail of the Earth. The major unresolved question is: Where does substorm onset occur, in a region closer to Earth or at a more distant location in the magnetotail. With the five Themis spacecraft the spatial propagation of the substorm associated magnetic field disturbance can be properly timed and its direction, tailward or Earthward, determined. Secondary science objectives are studies of magnetospheric processes such as the dynamic response of the magnetosphere to solar wind dynamic pressure variations, using the multi-spacecraft situation. This allows making use of special data analysis tools developed for the Cluster mission (e.g. Glassmeier et al. 2001).

The typical propagation speed of a substorm associated perturbation will be of the order of 1000 km/s and spatial scales of about 100 km are realistic. If a propagating structure with this scale and velocity passes a satellite it causes a temporal variation on a time scale of 0.1 s. Furthermore, in collisionless plasmas wave-particle interactions and thus also higher frequency plasma waves play an important role. In addition to the search coil magnetometer onboard the Themis spacecraft also the fluxgate instrument will provide important information about these waves. Baumjohann et al. (1999), for example, studied ELF waves in the frequency range 15–40 Hz using the fluxgate magnetometer onboard the Equator-S spacecraft. Amplitudes of the observed waves are of the order of 0.5 nT.

These and other science objectives enforce a couple of basic requirements to the magnetometer. First, the temporal resolution of the magnetometer should be at least 10 Hz and better. A second requirement needs to be imposed on the field resolution. Magnetic field changes associated with substorm processes will be as small as 1 nT. In order to trace the actual field variation of such small changes a resolution of at least 0.1 nT is required. Such a resolution is also suitable to observed higher ELF wave forms. A third requirement is imposed on the offset stability of the magnetometers. A key element of Themis measurements are coordinated observations at different locations within the magnetosphere. If, for example, substorm onset is triggered at a tail distance of 15 R_E and observed as close to the Earth as 5 R_E the time for the perturbation to travel this distance is of the order of minutes. During this time the offset should not change on the 0.1 nT level. This leads to a requirement for the offset stability of 0.2 nT/hour. A further requirement applies to the measurement range. Observations will also be taken close to Earth at fields levels of about 25,000 nT for attitude determination purposes. Thus, FGM needs to operate in a magnitude range between 0.1 and 25,000 nT.

3 Instrument Description

Fluxgate magnetometers are the most widely used magnetometers for space applications. The Themis fluxgate magnetometer FGM consists of a vector compensated three axis fluxgate sensor unit and a mainly digital electronics on a single printed circuit board. Magnetometer electronics and Power Control Unit share one of altogether five boards of the Instrument Data Processing Unit. Both, vector compensated sensor and sensor electronics, have flight heritage from magnetometers aboard the Rosetta Lander Philae (Auster et al. 2007) and VenusExpress (Zhang et al. 2006). The used ring cores—carrying the soft-magnetic material—are based on a 25 year-long continuous development phase carried out in Germany.

The special feature of the digital fluxgate electronics is the digitization of the AC output signal from the fluxgate sensor directly behind a preamplifier. It follows the general trend of a signal conversion from analog to the digital domain as close as possible to the sensor(s).

In this context, the replacement of analogue circuitry by digital processing in an FPGA improves the overall measurement stability, guarantees a precise timing of the field vectors relative to the system clock, independent from selected range and sampling rate, and furthermore reduces the susceptibility of the system to electro-magnetic interference. The feedback field in the fluxgate sensor is generated by two cascaded 12-bit Digital-to-Analog Converters (DACs). The field value is calculated by the sum of feedback field and measurement of the remaining field on the ring core position with a 14-bit Analog-to-Digital Converter (ADC). Both together provide field components with 24-bit resolution, which are transmitted to the Data Control Board (DCB).

The telemetry interface consists of two channels. The high telemetry channel (TMH) permanently provides 128 Hz samples and a low telemetry channel (TML) can be commanded to transmission rates between 4 and 128 Hz. The FGM output vectors are synchronized to a 1 Hz clock provided by the DCB. The DCB also contains the IDPU which shows responsible for all further processing of the FGM data like the generating of onboard data products as well as FGM controlling e.g. ranging. All secondary voltages (±8 V analog, ±5 V analog, +5 V digital and +2.5 V digital) required by FGM are provided by the Low Voltage Power Supply (LVPS) via the PCU.

Relevant housekeeping values are the temperatures of the sensor and the electronics as well as supply voltages and currents. Both temperatures sensor signals are conditioned on the magnetometer board and routed to the central housekeeping ADC as well as all power values.

The FGM resource requirements as well as its main instrument parameters are given in Table 1 and Table 2.

Table 1 Resources requirements

Mass	
Sensor	75 g
Harness	150 g (60 g/m)
Electronics	150 g
Dimensions	
Sensor	Diameter 70 mm, height 45 mm
Board	100 mm × 120 mm
Power consumption	800 mW
Data Interface to DCB	
TMH channel	128 Hz
TML channel	4–128 Hz; vector rate and filter mode are commandable
Data synchronization	Excitation frequency derived from IDPU clock; 128 Hz data centered to 1 Hz pulse

Table 2 Instrument parameters

Range	±25,000 nT
Resolution	3 pT (24bit)
Noise	$10\ \mathrm{pT}/\sqrt{\mathrm{Hz}}$ at 1 Hz
Temperature range/calibrated	
Sensor	−100° C…60° C
Electronics	−55° C…80° C
Offset stability	
vs. time	<1 nT/year
vs. sensor temperature	<50 pT/°C
vs. electronics temperature	<50 pT/°C
Gain stability	
vs. sensor temperature	22 ppm/°C (copper)
vs. electronics temperature	15 ppm/°C
Axes alignment	
Mechanical tolerance	<1°
Knowledge of axes direction	<1 arcmin
Stability of axes direction	<1 arcmin

3.1 Fluxgate Sensor

The ring-cores used for Themis have been developed by Karl Heinz Fornacon in Germany for more than 20 years (Müller et al. 1998). The main design goals have always been low noise and offset stability over a wide temperature range and period of time. Material selection and preparation as well as a proper thermal treatment are the key steps to achieve the performance parameters required for the Themis mission. The applied soft-magnetic material, a 13Fe-81Ni-6Mo alloy, is rolled to a foil of 20 μm thickness. Ribbons with a width of 2 mm are cut and 7 turns of it are wound on a bobbin made from Inconel. One of the most important permalloy parameters is the grain size which increases with the annealing temperature. The best noise results are achieved when the grain size is considerably smaller than the ribbon thickness (Fig. 1).

The selection of the ring-cores relies on an extended test procedure. After winding the excitation coil directly onto the ring core bobbins the noise of each ring core is measured before and after a specific aging process which consists of ultra sonic treatment, vibration, and temperature cycling. The sensor noise at 1 Hz of a ring core with a diameter of 13 mm is typically less than 5 $\mathrm{pT}/\sqrt{\mathrm{Hz}}$ as shown in Fig. 2.

After a pre-selection of those ring-cores with the lowest noise around 1 Hz, a quasi-longterm registration follows over a time period which must be longer than 1 day (typically one weekend) in order to verify the sensor noise at lower frequencies. This stability check is performed in a ferromagnetic shielding can. Several sensors are operated in parallel to

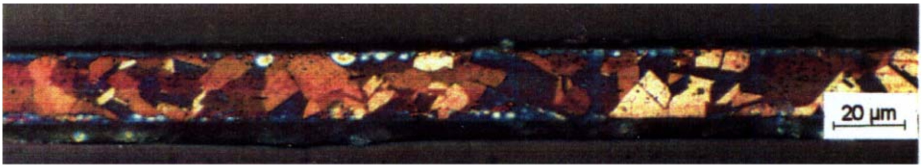

Fig. 1 Metallographic microstructure of the 13Fe-81-Ni-6Mo alloy annealed at 850°C (after Müller et al. 1998)

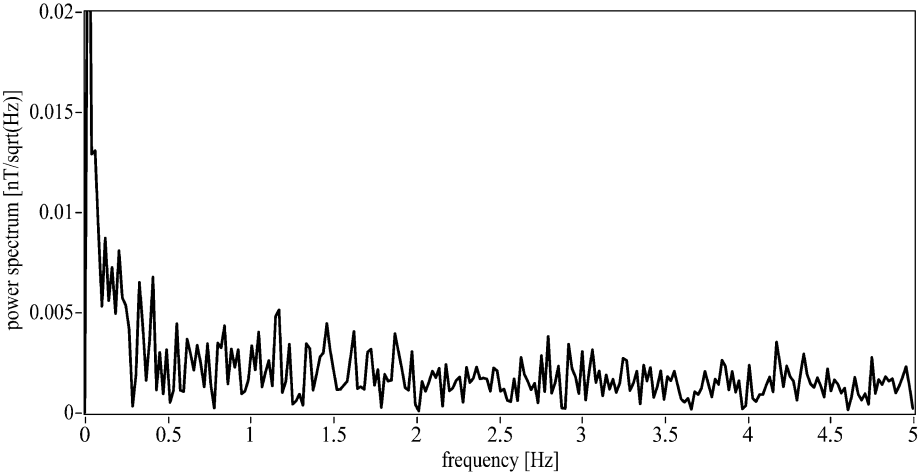

Fig. 2 Noise spectrum of a 13 mm ring-core as used for Themis

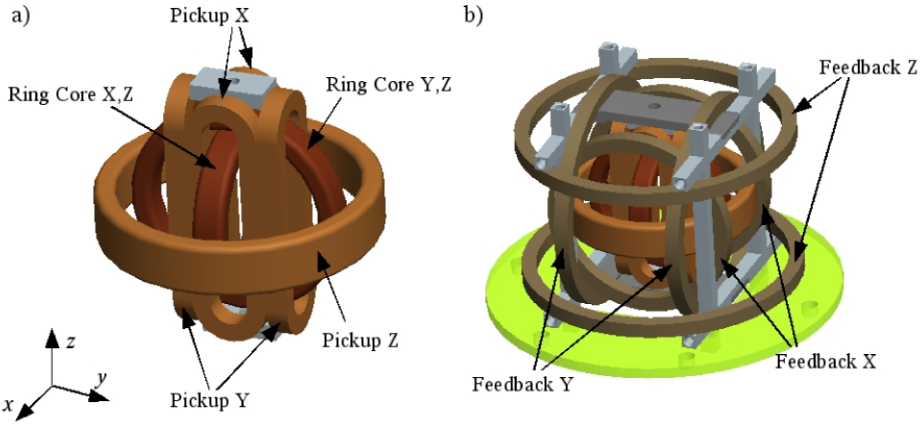

Fig. 3 3-D model of the FGM sensor with **a** ring cores and pick- up coil system and **b** fully functional sensor including the Helmholtz feedback system

separate the time and temperature dependence of the shielding can from ringcore related effects.

Two entwined ring-cores with a diameter of 13 and 18 mm are finally used to measure the magnetic field in three directions in the vector compensated sensor set-up. Via the smaller ringcore the magnetic field is measured in X and Z direction while the larger is used for Y and Z (see Fig. 3a). The ring-cores are equipped with two 3-D coil systems: an inner one to collect (pick-up) the magnetic field dependent second harmonic of the fundamental excitation frequency and an outer Helmholtz coil system to compensate the external field at the ringcore position. The pick-up coil system is attached as close as possible to the ring cores to increase the signal to noise ratio, in contrast to the comparably much larger Helmholtz coils which are used as feedback system to homogeneously compensate the magnetic field vector at the core position. The vector compensation keeps the sensitive sensor element in zero field. The single axis feedback design stabilized the scale value. The advantage of the vector compensation is the additional stabilization of the axis orientation. Thus both, scale value and axis direction depend only on the mechanically well stabilized feedback coil system. All coils are made from bond coated copper wire. By using this technology additional mechanical support, e.g. by ceramic rings, can be reduced to a minimum, the combination of materials with different thermal expansion coefficients can be avoided and mass can be saved. As a result, the mass of the sensor—excluding harness, mounting elements, protection cap and thermal hardware (see Fig. 3b)—could be reduced to less than 40 g for the type of sensor used for FGM.

3.2 Sensor Electronics

The block diagram of the FGM sensor electronics is shown in Fig. 4. An excitation AC current (excitation frequency at 8192 Hz, F0) drives the soft-magnetic core material of the two ring cores deep into positive and negative saturation. The external magnetic field distorts the symmetry of the magnetic flux and generates field proportional even harmonics of the excitation frequency in the pick-up coils.

In the digital fluxgate electronics design as used for FGM, analogue elements of traditional fluxgate magnetometers—such as filters and phase-sensitive integrators—are replaced

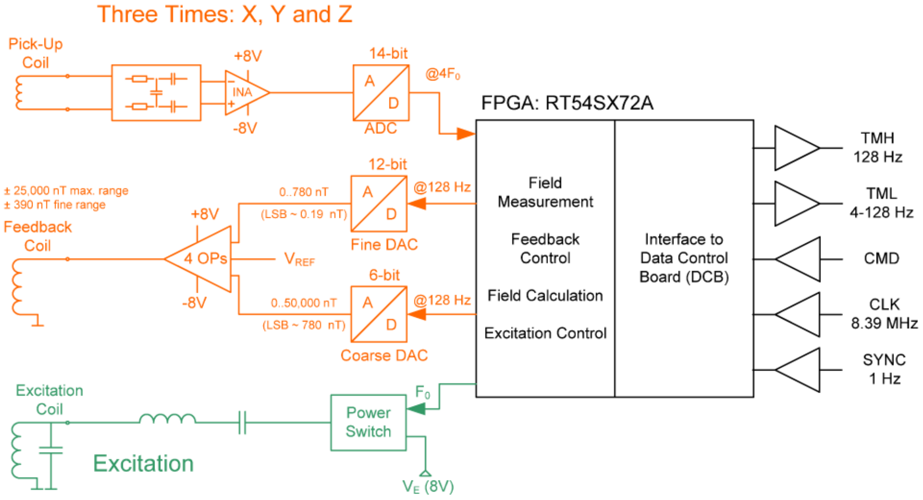

Fig. 4 Block diagram of the FGM sensor electronics

Table 3 Development steps of the digital magnetometer principle

Spacecraft mission	Control of ADC/DAC	Calculation of feedback	Calculation of magn. field	Type of FPGA
Rosetta/Lander	FPGA	DPU	DPU	RH 1280
VenusExpress	FPGA	FPGA	DPU	RT54SX32
Themis	FPGA	FPGA	FPGA	RT54SX72

by fast digitization of the sensor AC-signal and the subsequent data processing in FPGAs (Auster et al. 1995). Such a digital magnetometer was first development for the Rosetta Lander magnetometer followed by the magnetometer aboard the VenusExpress mission. From mission to mission the digital electronics has been further miniaturized as outlined in Table 3. In the ROMAP instrument, the near sensor FPGA mainly controls the converter components while the calculation of the feedback and the final output values are computed by a separate micro-processor (Auster et al. 2007). In the VEXMAG instrument aboard VenusExpress, the calculation of the feedback values is taken on by the FPGA (Zhang et al. 2006), and finally in the Themis FGM the complete digital processing is performed in a single near-sensor FPGA.

The replacement of analogue parts and the digitization on AC-level in general makes the sensed signal much more robust against changes of the environmental temperature and the supply voltage as well as insensitive to electro-magnetic interference, which are important features for the common E-box design of the Themis Instrument Data Processing Unit (IDPU).

The induced voltage in the pick-up coils is digitized behind the preamplifier at a sampling frequency of four times the excitation frequency. The accumulation of multiples of four consecutive data samples is necessary in order to eliminate all odd harmonics of the excitation signal, which couple from the excitation to the pick-up coil inductively. After processing the magnetic field digitally, the feedback settings are updated so that the field generated by the Helmholtz coil system compensates the external field almost completely.

The overall instrument performance is widely influenced by the sensor interface electronics. 14-bit ADCs (Maxwell 7872) and 12-bit DACs (Maxwell 8143) have been available with a radiation tolerant specification and reasonable power consumption for the Themis mission. The digital resolution of the 14-bit ADC at an input voltage range of ±5 V is 0.6 mV with a theoretically white quantization noise of 0.173 $\mathrm{mV_{RMS}}$. Considering a ratio of 256 between sampling (4F0, 32,768 Hz) and maximum output frequency (128 Hz), the quantization noise in the signal bandwidth is 10.8 $\mu\mathrm{V_{RMS}}$. With a nominal sensor sensitivity of 0.005 mV/nT and a pre-amplification of 40 dB—limited by the contents of odd harmonics in the pick-up signal—the amplitude of the digitization error is in the order of 21.6 $\mathrm{pT_{RMS}}$ for a signal bandwidth of 64 Hz which corresponds to a noise density of less than 3 $\mathrm{pT}/\sqrt{\mathrm{Hz}}$ assuming a white noise behavior. Thus, the digitization error does not exceed the design goal of 10 $\mathrm{pT}/\sqrt{\mathrm{Hz}}$ at 1 Hz. Nevertheless it is in the order of the sensor noise as shown in Fig. 2 and cannot be neglected completely.

More critical is the limited resolution of the DACs and here especially the non linearity which is in the order of half a Least Significant Bit (LSB). This corresponds to a non acceptable 6 nT error if one DAC is used for the whole measurement range of ±25,000 nT. Therefore two 12-bit DACs are cascaded (as shown in Fig. 4), a coarse one with a range of 50,000 nT (only the upper six bit active with the lower bits constantly set to binary 100000) and a fine one with a 780 nT range. The output voltages of the cascaded DACs are connected to a voltage to current conversion circuit. Using the fine DAC for the scientifically relevant low field range only, the maximum non linearity error for this range could be limited to <0.23 LSB and corresponding <43 pT by a pre-selection process of the best DACs. For fields above 400 nT (used for attitude determination) the linearity error of the coarse ADC has to be taken into account. During data post-processing on ground the non-linearity is partly corrected (MSB only). This is done before calibrating data inflight, because an uncorrected non-linearity of 2×10^{-4} would limit the accuracy of determination of scale value ratios and angle errors.

The core of the digital fluxgate electronics is an RT54SX72 FPGA from Actel. Its functionality can be divided into three sections: interface to sensor, interface to DCB and a 32-bit RISC processor module especially designed for the Themis magnetometer (see Fig. 5).

The sensor interface module enables the excitation; it starts the ADC sampling with programmable phase shift versus excitation clock at all three channels synchronously, averages (sign sensitive) a programmable number of ADC values and sends the results to the processor module. The processor calculates the magnetic field vector by adding the old DAC and new ADC values, both scaled by programmable conversion factors k_1 and k_2. Additionally, new feedback settings are calculated and passed to the sensor interface. High resolution 128 Hz data and low resolution low pass filtered or decimated data (4–128 Hz) are transferred via output register to the DCB interface. The DCB interface module receives commands for configuring hard- and software, synchronizes the data sampling to all other scientific instruments by a 1 Hz clock, and sends the serial data stream to the DCB containing the magnetic field vector (3×24 bit word) and a status word. In Table 4 all programmable configuration settings are listed.

Using these settings the instrument can be commanded into various modes. In the standard mode magnetic field values are calculated using commanded scaling factors. Lower time resolution data (TML) are calculated by filtering the raw data with a non-overlapping arithmetic averaging filter, by data decimation or a combination of both. For health checks,

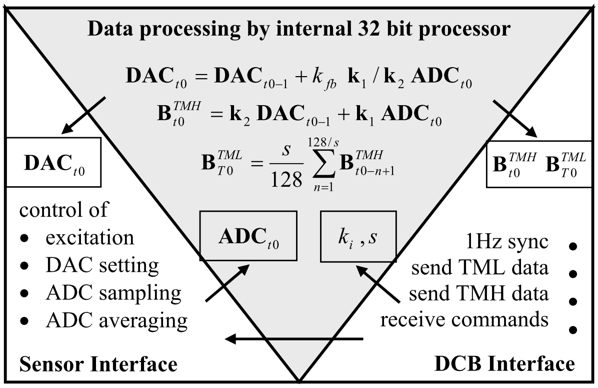

Fig. 5 Block diagram of the magnetometer FPGA. The magnetic field vector **B** is calculated by sum of the active ADC values and previous DAC settings. The factors k1 (ADC's) and k2 (DAC's) change converter units into magnetic field values with a basic resolution of 3 pT. The most significant bit of the DAC corresponds to a feedback field of 25,000 nT. The resulting field (24-bit) is transmitted via High Telemetry (TMH) and simultaneously after averaging via Low Telemetry (TML) to the Data Control Board (DCB)

Table 4 Summary of configurations settings

Hardware configurations	Excitation on/off Feedback on/off Relays on/off Type of filter
Software configurations	Sampling setup (phase, number) ADC/DAC scaling factors ki & offsets Fixed DAC values TML telemetry rate TML filter type

analysis of error sources and in the case of malfunctions in the feedback circuitry the feedback loop can be opened by software (open loop command) or hardware (relays). In this case all three k_2 values have to be set to zero.

Three calibration modes can be commanded by setting hard- and software options. In Cal-1 mode the instrument is operated in an open loop regime and the DAC values can be commanded manually. By this method the sensitivity of a sensor can be checked. Applying a constant calibration field and varying the phase between excitation and ADC sampling the balance of sensor and electronics input impedance can be checked and if necessary readjusted.

In Cal-2 mode the DAC setting are incremented automatically. This mode can be used to check the linearity of the sensor. Counting range as well as exposure time can be configured. If the sensor output is ignored ($k_1 = 0$) and the DAC values are not scaled ($k_2 = 1$), the count steps are transmitted directly. In this case the magnetometer generates independently from the external magnetic field a step function which can be used to check further data processing steps, telemetry quality and data timing. In Cal-3 mode ADC and DAC values are transmitted separately in TMH and TML channels. The mode is used to analyze the control behavior of the feedback loop.

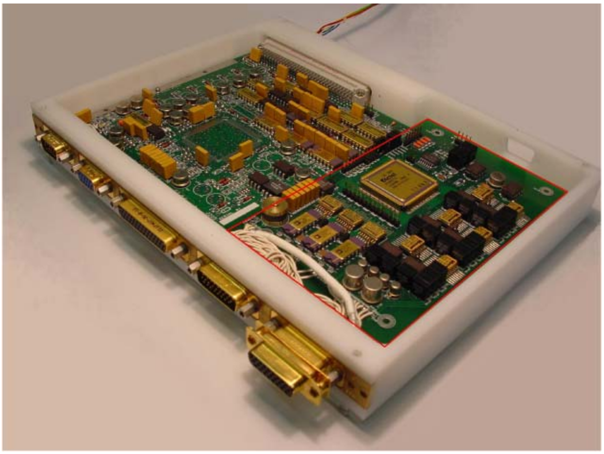

Fig. 6 Themis FGM electronics (*red square*) placed on a shared board

The electronics with the described functionality is placed on one side of a Themis standard board (see Fig. 6). The FGM board area is about 120 cm^2, the power consumption is 800 mW and its mass adds up to 150 g.

3.3 Onboard Data Processing at IDPU

The FGM electronics sends data over a serial interface to the processor board (DCB) inside the IDPU. Here the IDPU Flight Software (FSW) processes and packetizes the data. The 24 bit long vectors are shifted to select only 16 bits for telemetry. The selection of which 16 bits acts as a ranging function by selecting the widest range with the lowest resolution up to the smallest range with the highest resolution. As the samples are stored in memory, a header is written to the packet that includes the FGM message from the FGE board and the range and sample rate data (in the case of the variable rate packet). The packet timestamp is also added to this header when the packet is created and consists of time in seconds since January 1st 2001 as a 32 bit quantity and 16 bits of subseconds. Two separate telemetry streams are sent to the DCB board from the FGM. One is constant, 128 Samples/s data known as TMH and the other is variable rate data from 4–128 Samples/s known as TML. The FSW also takes the TMH stream and samples it to produce the attitude control packet that provides 8 Hz magnetometer data for spacecraft mission operations. This data is always in the widest least sensitive range. Two temperatures are sampled from the FGM thermistors, one on the FGE board and the other on the sensor. These, along with the FGM control word and message are reported in IDPU housekeeping.

The IDPU FSW also samples the FGM telemetry stream to process onboard spin fitted data. This is downlinked as a separate packet to the time series data. The software collects samples from the B-field vectors by taking 32 points at equal angles and fitting a sine wave least squares fit to the data. The best fit of the data is defined by the formula: $A + B \times \cos() + C \times \sin()$. The spin fit process calculates the least square fit and its standard deviation and then rejects the points that are far from the fit. The calculation is repeated until no more points are rejected. The fit can be chosen to be on the Bx or By data. Given a spin rate of 3 seconds, the use of 128 Hz data for spin fitting puts an apparent phase shift of $360/(3 \times 128)$ or roughly 0.9 degrees into the results. While this meets the 1.0 degree requirement, the phase shift correction can be determined on the ground using the spin pulse time data relative to the 1 Hz tick which is the basis of the 128 Hz data. In addition, the FSW averages the Z-axis data and provides it in the spin fit packet.

4 Instrument Calibration

4.1 Determination of Transfer Function

To measure the magnetic field vector correctly the magnetometer output ($\mathbf{B}_{\mathrm{out}}$ in digital units) has to be scaled in nT, offset corrected and transferred into an orthogonal system. Assuming a diagonal matrix ($\mathbf{M}_{\mathrm{gain}}$) to convert the digital units into nT, an offset vector ($\mathbf{O}_{\mathrm{fgm}}$) and a matrix ($\mathbf{M}_{\mathrm{ort}}$) to transform the measured components into an orthogonal system the calibrated field vector ($\mathbf{B}_{\mathrm{fgs}}$) can be written as follows:

$$\mathbf{B}_{\mathrm{fgs}} = \mathbf{M}_{\mathrm{ort}}(\mathbf{M}_{\mathrm{gain}}\mathbf{B}_{\mathrm{out}} - \mathbf{O}_{\mathrm{fgm}})$$

The dependence of these parameters on field magnitude, field dynamics, time and temperature shall be investigated by the calibration procedure. The offset is field independent per definition. If sensor and electronics are well balanced the offset should also not depend systematically on sensor and electronics temperature. The design goal is to keep the non systematic variation low, the goal of calibration is to record its behavior. To get a sufficient statistics, the offset was measured by sensor rotation in a weak field as often as possible, typically in the beginning and end of each calibration campaign. The determination of its temperature dependence was part of the test described in the following section.

The scale values in contrast are well defined by the feedback design. To investigate its temperature behavior, the expansion coefficients of the feedback coils and thermal coefficients of electrical parts have to be studied. Additionally its field and frequency dependency must be considered. The field non-linearity mainly caused by the DACs is discussed in Sect. 3.2, the frequency dependency later in this section. Due to the possibility to actualize the scale values by modification of k values, scaling ($\mathbf{B}_{\mathrm{fs}} = \mathbf{M}_{\mathrm{gain}}(k)\mathbf{B}_{\mathrm{out}}$) can already be done onboard by the magnetometer software.

Cross coupling between magnetic axes caused by the electronics can be neglected due to the digital design. Therefore the misalignment is in contrast to sensitivity and offset a pure sensor property. Tests have been done to prove this assumption. If the orthogonality depends on the sensor only, arbitrary digital fluxgate electronics can be used for determining the orientation of magnetic sensor axes. To perform a scalar calibration the range of the qualification electronics has been extended to ±50,000 nT. The Earth field vector was measured at various sensor orientations and the calculated field magnitude has been compared to the field measured by a proton magnetometer. As derived by Auster et al. (2002) the motion about two sensor axes would be sufficient to provide the coefficients of a linear transfer function by this method. Measurements at arbitrary orientations, in practice at 24 sensor position which can by reached by 90° rotation of a cube, provide a sufficient redundancy. By this method the three angles of non-orthogonality were determined. In a second step the sensor was mounted in a fixture representing an orthogonal coordinate system with high precision (see Fig. 7).

The mechanical reference system of the fixture is defined by 6 center holes. By these holes the fixture can be pivoted along the three coordinate axes. If the rotation axis is oriented approximately perpendicular to the Earth field vector (e.g. in magnetic east-west direction), a misalignment of the true sensor axis to the reference axis causes a sinusoidal signal in the magnetic field measurement if the fixture is rotated about the reference axis. The sine amplitude normalized by the total Earth field and the phase versus Earth field direction provide the absolute misalignment of the true sensor axis. If the rotation is performed about all three axes of the reference system, all six angles of a transformation into the reference

Fig. 7 Sensor in fixture which defines the mechanical reference system with a precision of 10 arcsec

Fig. 8 Sensor fixation on boom for repeatable sensor mounting

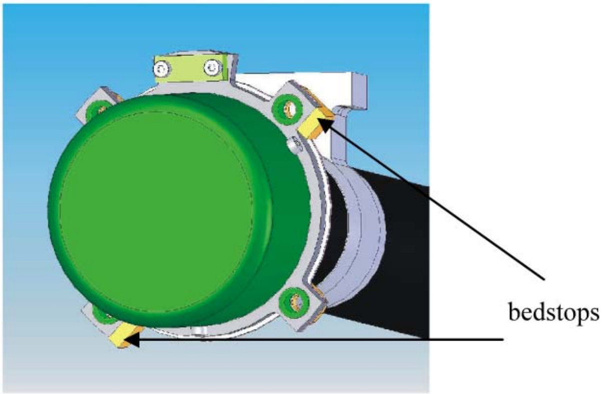

system are determined. These six angles include the three angles of non orthogonality, which can be used to verify the first step, and additionally the rotation into the reference system.

Finally, the orientation of the sensor with respect to the probe has to be determined. The sensor interface is well defined by the mounting plane and two bedstops (see Fig. 8). This interface permits the repeatable mounting and demounting of sensors to the boom and in test facilities. The orientation of the sensor interface versus boom as well as the orientation of the boom vs. probe was measured by means of geodetic instruments in stowed and deployed boom configuration at the UCB workshop. This measurement completes the chain from raw data in a non orthogonal sensor system to a calibrated field vector in the probe system.

The only frequency dependent calibration quantity is the scale value. The sensor output signal is digitized exactly at the maximum and minimum of the second harmonic of the excitation signal with an sampling rate of 32,768 Hz. A certain number N of ADC samples are accumulated to one output value 128 times per second in order to produce the 128 Hz FGM raw data. To avoid the measurement during feedback updating, data sampling and feedback setting have to be done sequentially. Taking into account the time for the feedback calculation as well as the stabilization of the feedback current, only 232 samples of the maximum number of $N_{\max} = 256$ are accumulated. The frequency characteristic of the accumulated data is that of a standard average (boxcar) filter without overlapping. The fre-

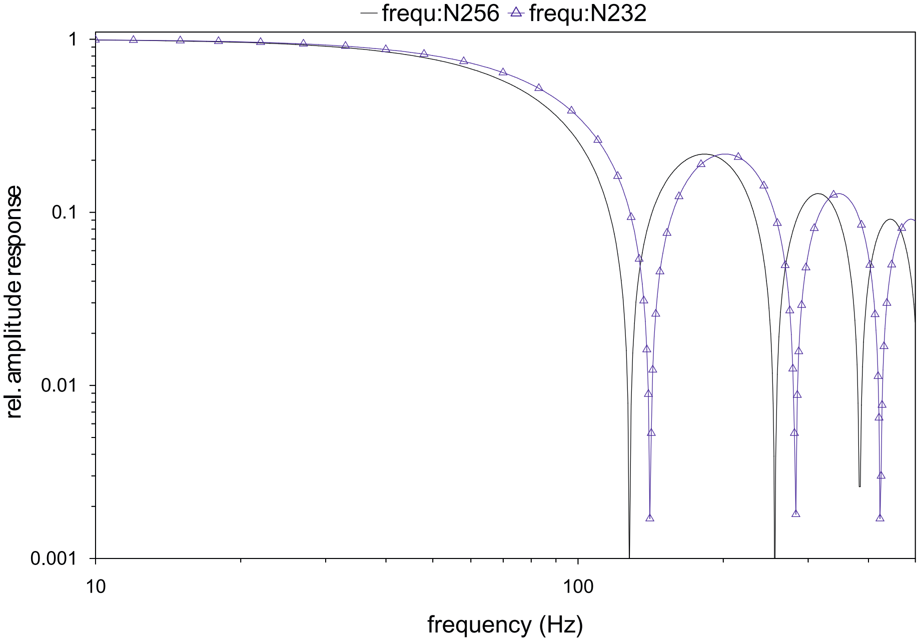

Fig. 9 Amplitude response of 128 Hz data

quency response of the averaging filter can be expressed analytically by amplitude $G(w)$ and phase $a(w)$ response:

$$G(\omega) = \frac{\sin(0.5N\omega T)}{N\sin(0.5N\omega T)}, \qquad \varphi(\omega) = -0.5N\omega T$$

where $\omega = 2\pi f$ denotes the angular frequency and T the sampling period (1 s/32,768).

Figure 9 shows the amplitude response for maximum ($N = 256$) and real ($N = 232$) samples accumulated. The filter characteristic of the sequential sampling mode is shifted by 13.24 Hz to higher frequencies. A verification of the frequency response has been done by measurements in Graz applying sine wave fields between 0.1 and 180 Hz generated in calibration coils. Amplitude and phase are measured with respect to the field generating current.

Low telemetry data are derived from 128 Hz raw data by averaging data using a non overlapping boxcar filter. Note that the DC field value is affected due to spin modulation by the filter characteristics. This has to be corrected during ground data processing.

4.2 Dependency on Electronics and Sensor Temperature

The test of the dependency of instrument parameter on electronics temperature was performed at TU-Braunschweig. The electronics boards were mounted inside a temperature chamber in which the temperature has been varied between −20 and +60°C. The sensor was placed in the Themis sensor Control Unit (TCU), a ferromagnetic shield, in which the Earth field is suppressed by a factor of 10^4. The TCU is equipped with a coil system (see Fig. 10) to generate test fields and a rotation capability to check the sensor offset.

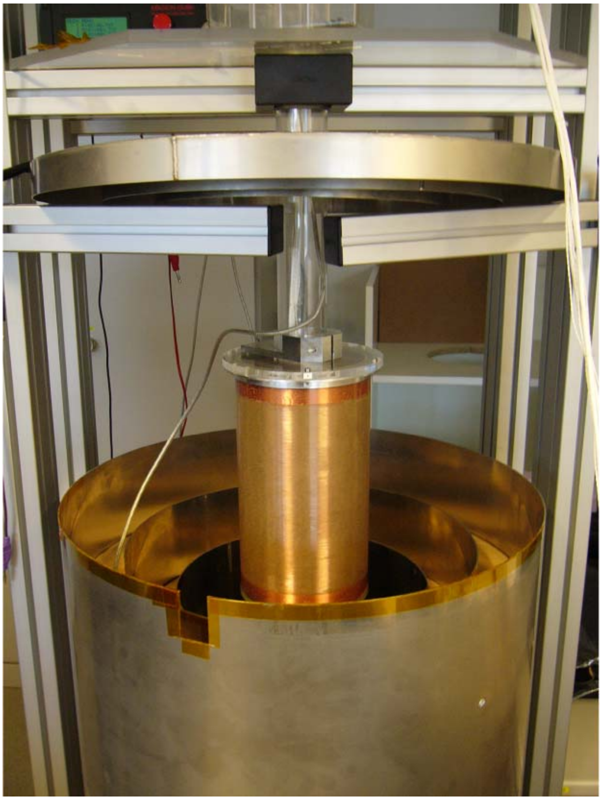

Fig. 10 TCU with coil system and sensor rotation capability

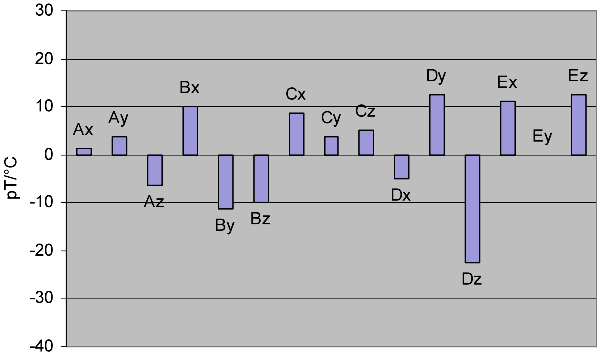

Fig. 11 Offset drift depending on electronics temperature of all sensor components (Probe A-E) caused by excitation and pick-up electronics

The dependency of the scale values on electronics temperature was tested by applying 20,000 nT in each vector direction. For each electronics channel a temperature sensitivity of less than 5 ppm/°C could be diagnosed. No measurable changes could be detected for linearity, noise, phase of second harmonics versus excitation clock and inrush current. The changes in power consumption are less than 5% in the tested temperature range.

Offsets are measured by rotating the sensor inside the screen. Due to the possibility to open the feedback, the sources of a changing offset could be separated into excitation and pick-up electronics (if feedback relays are open) and feedback current. Excitation and pick-up contribute to the temperature drift with less than ±20 pT/°C (see Fig. 11), the feedback

Fig. 12 Offset drift depending on electronics temperature of all sensor components caused by feedback circuitry

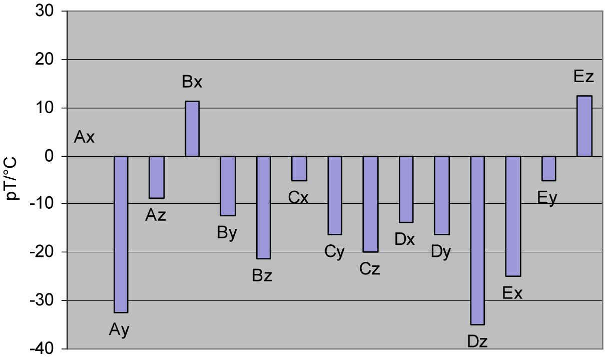

Fig. 13 Facility to measure the dependency of instrument parameters on sensor temperature

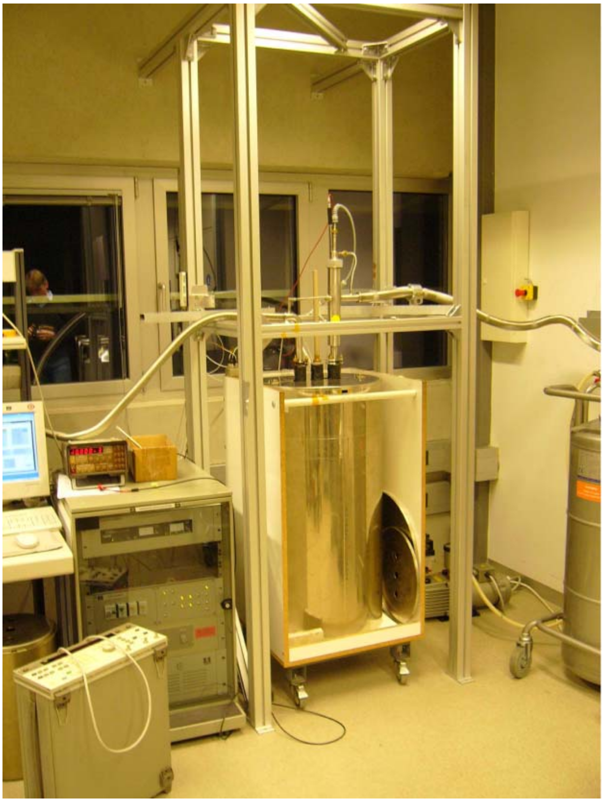

current instead shows an averaged negative temperature coefficient of -10 pT/°C with an error bar of ±20 pT/°C (see Fig. 12).

The dependency on sensor temperature was tested in a ferromagnetic shield equipped with a liquid nitrogen controlled temperature chamber (see Fig. 13) at IWF Graz in a temperature range between -100°C and $+65$°C. The tests showed that the noise levels (measured at 1 Hz) become higher at lower sensor temperatures. While FGM has a typical noise of 10 pT/$\sqrt{\text{Hz}}$ at temperatures between 0°C and 60°C, the noise increases from 15–20 pT/$\sqrt{\text{Hz}}$

at temperatures about $-50°\text{C}$ up to 30 $\text{pT}/\sqrt{\text{Hz}}$ at $-100°\text{C}$ which is still within the specifications. The expected sensor temperature in the Earth orbit is around 0°C.

Even as the temperature dependency of noise is an unintentional effect, properties like sensitivity or phase of sampling vs. excitation change inevitably with temperature. The permeability of the core and hence the inductivity of the pick up coil as well as its resistance are functions of the temperature and affect the balance conditions of the input circuitry. The advantage of the digital magnetometer is, that these effects can be determined and compensated by updating the instrument configuration (phase shifts, scaling factors). Figure 14 shows the input sensitivity versus ADC sampling phase at three temperatures. The phase shift changes due to the temperature dependent inductivity of the ringcore. The sensitivity at lower temperature increases due to the lower copper resistance.

Current sources are used to drive the feedback, therefore the sensitivity shall depend only on the thermal expansion coefficient and not on the resistance of the feedback coil system. Only materials with expansion coefficients of about 20 ppm/°C (aluminum, copper) are used. All sensitivity measurements confirm this temperature coefficient within an error bar of ±3 ppm/°C. Due to the fact that combination of materials with different expansion coefficients are avoided (e.g. copper and ceramics) the temperature coefficient is constant over the whole temperature range.

Offsets are measured by sensor rotation at various temperatures. Also the offset dependency on sensor temperature is comparable to the one of the electronics temperature (<30 pT/°C). Figure 15 shows, that no systematic temperature behavior is noticeable.

4.3 Parameter Check under Well-Defined Field Conditions

Two tests were done to check the overall functionality and to verify the calibration parameters. First the magnetometer was tested by artificial fields generated in a coil system, and secondly by variations of the Earth field.

The sensors were mounted inside a thermal control box, which is placed in the coil center (see Fig. 16). After the setup measurements (standard mode, 4 Hz data rate, external field ±20000 nT) the calibration was started with a test field sequence at 20°C. Then the temperature was increased to 60°C with a gradient of 0.3°C/min and the measurement sequences were repeated. The cooling down to about $-70°\text{C}$ was performed using ceramic blocks (3.5 kg) which had been cooled in liquid nitrogen prior measurement. At all temperature levels sensitivity and orthogonality were checked.

The direct comparison between two instruments or if possible the comparison with an observatory magnetometer is an expedient method to verify the properties of the instrument. Two Themis sensors are respectively mounted on a pillar (see Fig. 17) and compared with a reference instrument. Unfortunately the earth field vector on ground cannot be measured by the Themis magnetometer because its range is adjusted for a perigee of more than 1000 km. Therefore, only the horizontal components are compared. The test was repeated with a sensor alignment rotated by 90°.

Sensors of observatory and Themis magnetometers are identical. The reference electronics, usually applied in geomagnetic observatories, can be used as standard because it is well tested and has no limitations due to the space restricted part assortment. The tests were performed in the Test Facilities of Magson GmbH in Jeserigerhuetten (Germany). First of all, irregularities like field jumps, data loss, timing problems etc. can be detected. Furthermore, the long term behavior, including stability of offsets, scale values and magnetic axes can be evaluated and finally, as shown in the extracted short term pulsation registration (see Fig. 18), it is an in situ test of measurements of field changes expected during substorm onsets.

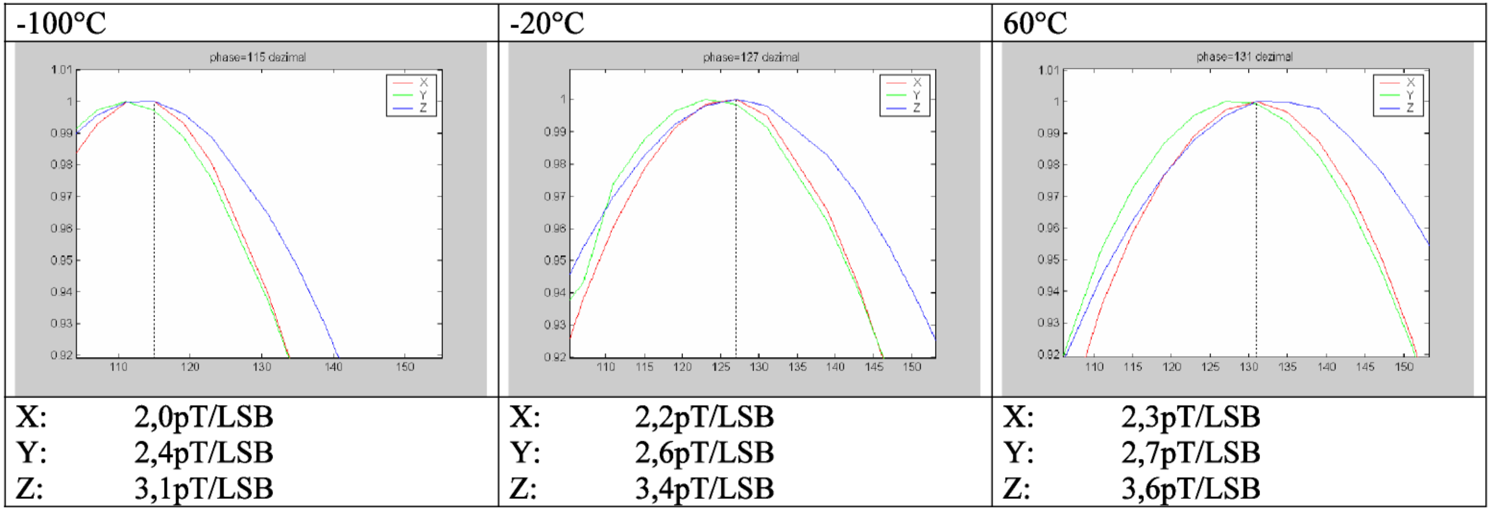

	-100°C	-20°C	60°C
X:	2,0pT/LSB	2,2pT/LSB	2,3pT/LSB
Y:	2,4pT/LSB	2,6pT/LSB	2,7pT/LSB
Z:	3,1pT/LSB	3,4pT/LSB	3,6pT/LSB

Fig. 14 Input sensitivity and phase of ADC sampling versus excitation clock in dependency on sensor temperature. *Upper panel* show the sensitivity versus phase angle, the numbers *below* provide the sensitivities absolutely

Fig. 15 Offset drift depending on sensor temperature of all sensor components

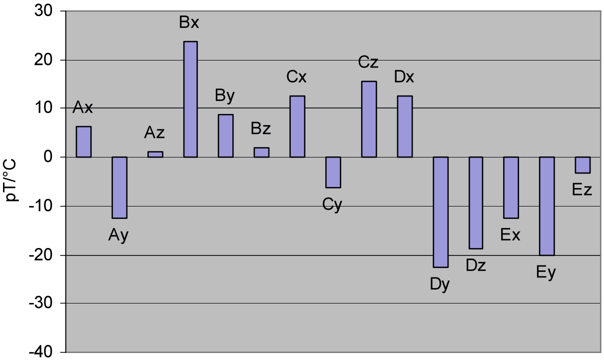

Fig. 16 Coil system with thermal box baseplate in Magnetsrode, Braunschweig

Fig. 17 Two Themis sensors mounted on a pillar to measure Earth field components for comparison with an observatory instrument

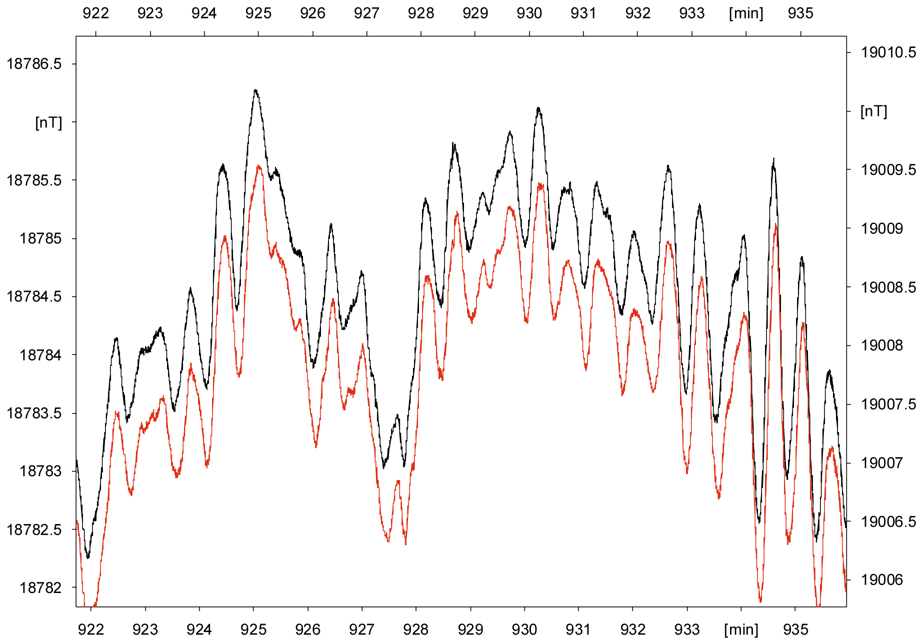

Fig. 18 Pulsation measurement of two Themis magnetometers (*black* THC, *red* THD) performed in north-south direction of the Earth field. Field variations measured with an independent observatory instrument confirm the result of both Themis magnetometers

4.4 Parameter Check during S/C Integration (SFT)

The integration took place in Berkeley. Effects on measurement quality had to be expected. The second half of the board (PCB) was powered for the first time together with the FGM electronics, the secondary voltages were provided for the first time by the original DC/DC converter, and finally the interface to DCB was established. This made the precise magnetic field measurement at the integration environment necessary. Especially, parameters like noise and offset had to be checked routinely before and after integration steps.

A test facility which protects the sensor from Earth and technical field variations and which is mobile enough to follow the magnetometer during its integration procedure was used. Three of the ferromagnetic shields which were already used to keep the sensor in a controlled environment during electronic temperature tests (see TCU description in Sect. 4.2) are installed in Graz, Braunschweig and Berkeley. The Berkeley unit was used for all tests before and after integration steps. During the tests the sensor was removed from the boom and placed inside the TCU, connected by an extension cable. The influence of the extension cable on calibration parameters has been tested and stated as negligible.

A Short Functional Test (SFT) procedure of 20 minutes duration, performed by the integration team, checks the overall functionality, offsets, scale values, noise, sensor-electronics balance and telemetry errors. Each instrument was tested during the s/c integration about 20 times by this procedure. As a result we found two errors—a sensor was replaced due to increased noise level, a cable short was detected and removed—and it provided statistics of the tested parameters covering more than one year. Although S/C induced disturbances were investigated by these tests, some interference could only be identified in space as shown in Sect. 5.2.

Table 5 Coordinate systems which are used to transform the magnetometer output data into a spin aligned sun oriented system as defined in detail in Angelopoulos (2008). Abbreviations are referred to the terms used for Cluster

Abbreviation	Description
FS	Non orthogonal sensor system
FGS	Orthogonal sensor system
UNIT	Boom aligned system
SPG	Spinning Probe Geometric
SSL	Spinning Sunsensor L-oriented
DSL	Despun Sun oriented L-oriented

4.5 Creation of Calibration Files

In the following sections calibration relevant coordinate systems are introduced and the creation of CalFiles is described. Elements of the calibration matrix are derived from many individual parameters which can be clearly related to instrument/spacecraft properties.

The magnetometer provides data in digital units in a non orthogonal coordinate system (FS). The digital units are pre-scaled by the magnetometer processor. The conversation factor of 2.98 pT/bit is specified by the ratio between dynamic range (±25,000 nT) and digital resolution (24 bit). The selection of the transmitted 16 bit is done by the so-called ranging in the IDPU. Range 8 stands for transmitting the lower 16 bits, range 0 for transmitting the upper ones. The range dependent conversion factor can be expressed by: $k_r = 50{,}000/2^{(16+\text{range})}$. The sensor offsets $\mathbf{O}_{\text{fgm}}$ have to be corrected in the FS system and the data has to be transformed by $\mathbf{M}_{\text{ort}}$ into an orthogonal sensor system (FGS):

$$\mathbf{B}_{\text{fgs}} = \mathbf{M}_{\text{ort}}(k_r \times \mathbf{B}_{\text{fs}} - \mathbf{O}_{\text{fgm}})$$

The orientation of the sensor coordinate system is defined by the mechanical interfaces of sensor and boom (see Fig. 19) as well as by the moment of inertia of the probe which determines the rotation axis. All angles of these three coordinate transformations are measured on ground. The determination of the sensor alignment versus boom interface ($\mathbf{M}_{\text{unit}}$) is part of the sensor calibration program, the boom alignment versus spacecraft ($\mathbf{M}_{\text{probe}}$) is measured during the boom verification procedure. Using these coordinate transformations, the magnetic field data can be rotated into the probe coordinate system:

$$\mathbf{B}_{\text{spg}} = \mathbf{M}_{\text{probe}}\,\mathbf{M}_{\text{unit}}\,\mathbf{B}_{\text{fgs}}$$

In the probe coordinate system errors caused by the magnetic properties of the spacecraft are considered. Spacecraft offsets $\mathbf{O}_{\text{sc}}$ are added. The influence of probe soft-magnetic material on the direction of the sensor axes can be neglected, its influence on the sensitivity is compensated by multiplying the magnetic field with $\mathbf{M}_{\text{scale}}$. To align the coordinate system with the spin axis and to align the x axis with the sun direction, the field vector has to be rotated by $\mathbf{M}_{\text{spin}}$ and $\mathbf{M}_{\text{phase}}$. The nominal spin axis and spin phase alignment are determined during the spin balance tests at JPL and the sun sensor integration. Additionally the delay and the spin dependent damping factor of the boxcar filter for TML data has to be compensated. This is done by $\mathbf{M}_{\text{filter}}$ which contains the rotation about the angle α_{delay} for the filter delay and the correction of the sensitivity in the spin plane of d_{filter}:

$$\alpha_{\text{delay}} = -\pi\,\frac{f_{\text{spin}}}{f_{\text{sample}}}; \quad \text{and} \quad d_{\text{filter}} = \frac{f_{\text{sample}}}{128}\,\frac{\sin(\frac{\pi}{128}f_{\text{spin}})}{\sin(\pi\,\frac{f_{\text{spin}}}{f_{\text{sample}}})}$$

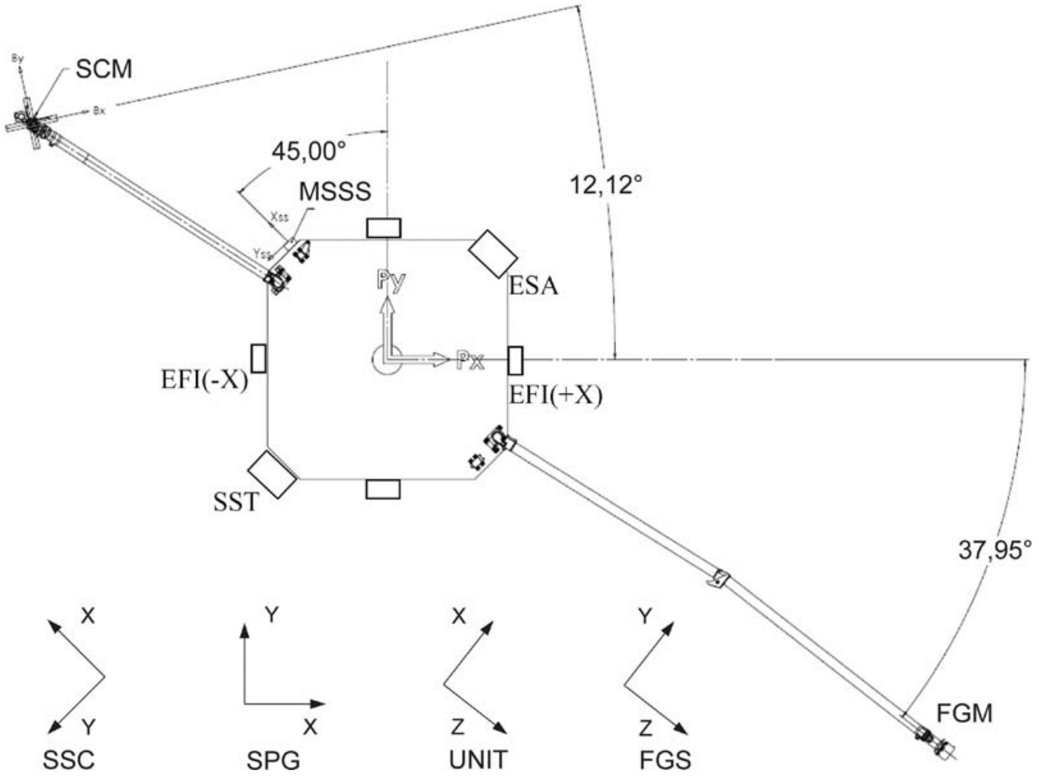

Fig. 19 Accommodation of boom mounted FGM sensor and orientation of instrument, boom, probe and sun sensor (MSSS) related coordinate systems

The magnetic field in the spin aligned sun oriented system can be calculated by:

$$\mathbf{B}_{\mathrm{ssl}} = \mathbf{M}_{\mathrm{filter}}\,\mathbf{M}_{\mathrm{phase}}\,\mathbf{M}_{\mathrm{spin}}\,\mathbf{M}_{\mathrm{scale}}\,(\mathbf{B}_{\mathrm{spg}} - \mathbf{O}_{\mathrm{sc}})$$

The calibration File contains all corrections/transformation up to the SSL-system. Calibration matrix $\mathbf{M}_{\mathrm{cal}}$ and offset $\mathbf{O}_{\mathrm{cal}}$ are calculated by the single transformations as follows:

$$\begin{aligned}
\mathbf{B}_{\mathrm{ssl}} &= \mathbf{M}_{\mathrm{filter}}(\mathbf{M}_{\mathrm{cal}} k_{\mathrm{r}} \times \mathbf{B}_{\mathrm{fs}} - \mathbf{O}_{\mathrm{cal}}) \\
\mathbf{M}_{\mathrm{cal}} &= \mathbf{M}_{\mathrm{phase}}\,\mathbf{M}_{\mathrm{spin}}\mathbf{M}_{\mathrm{scale}}\,\mathbf{M}_{\mathrm{probe}}\,\mathbf{M}_{\mathrm{unit}}\,\mathbf{M}_{\mathrm{ort}} \\
\mathbf{O}_{\mathrm{cal}} &= \mathbf{M}_{\mathrm{phase}}\,\mathbf{M}_{\mathrm{spin}}\,\mathbf{M}_{\mathrm{scale}}(\mathbf{M}_{\mathrm{probe}}\,\mathbf{M}_{\mathrm{unit}}\,\mathbf{M}_{\mathrm{ort}}\,\mathbf{O}_{\mathrm{fgm}} + \mathbf{O}_{\mathrm{sc}})
\end{aligned}$$

$\mathbf{M}_{\mathrm{filter}}$, $\mathbf{M}_{\mathrm{probe}}$, $\mathbf{M}_{\mathrm{unit}}$ and $\mathbf{O}_{\mathrm{fgm}}$ are assumed to be constant. Their values are determined by ground calibration. $\mathbf{M}_{\mathrm{phase}}$, $\mathbf{M}_{\mathrm{spin}}$, $\mathbf{M}_{\mathrm{scale}}$, $\mathbf{M}_{\mathrm{ort}}$ and $\mathbf{O}_{\mathrm{sc}}$ are time dependent and therefore subjects to the inflight calibration procedure. Initial values are taken also from ground calibration.

5 First Results

5.1 Inflight Calibration Result

During commissioning all basic functions are tested by a procedure similar to the one applied for short functional tests on ground. Some modifications are necessary due to the rotation period of the probes. Sensor-electronics balance and sensitivity are unchanged compared to preflight tests, telemetry quality and onboard data processing are error free. The tests have been repeated after the successful deployment of all magnetometer booms. After deployment the total noise level of the magnetic field measurement was checked at apogee crossings. A statistic about the noise level of all 15 sensors is shown in Fig. 20.

The number of sensors was counted for certain noise levels. At 1 Hz the averaged noise level of all 15 components is about 12 pT/$\sqrt{\mathrm{Hz}}$, which is less than half of the required level of 30 pT/$\sqrt{\mathrm{Hz}}$. Based on the results of the preflight calibration (see Sect. 4.1) we can assume a linear transfer function between the magnetometer output in a non orthogonal sensor

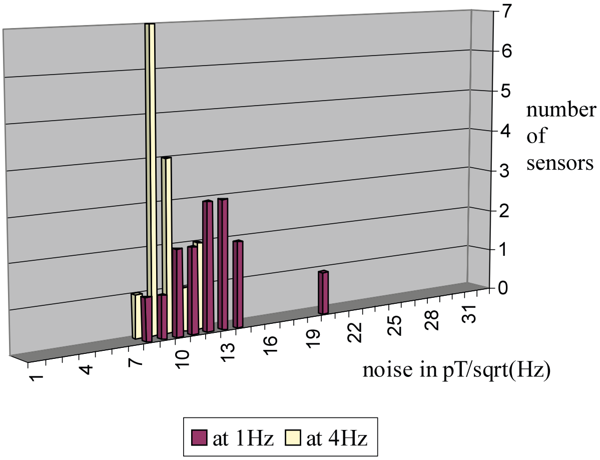

Fig. 20 Noise Statistic measured inflight: The overall noise was measured for each sensor at quiet field conditions. The sensors are sorted by noise levels at 1 Hz and 4 Hz. A noise level less than 30 pT/$\sqrt{\mathrm{Hz}}$ at 1 Hz was required

system and the magnetic field vector in a spin axis aligned spacecraft system. Updating the initial elements of the transfer function at regular intervals is a task of the in-flight calibration. The result of the in-flight calibration is a calibration file (CalFile) which contains the 12 elements of the vector transformation, the spin period and the time of validity.

The elements of the transformation consist of scale values, non-orthogonality, sensor orientation and offsets. Deviations from nominal values are caused by many reasons, either constant in time (e.g. boom and sensor alignment) or time and temperature dependent (e.g. sensor and spacecraft generated offsets).

To determine the transfer function in flight we need a multitude of inputs. First the rotation of the spacecraft can be used. The fact that the spin frequency and its first harmonic have to be absent in the field magnitude provides 4 equations. Furthermore one axis is defined by the spin axis (2 equations). 8 of 12 elements are affected by the spacecraft rotation namely two spin plane offsets, the ratio between spin plane scale values, all three angles of non-linearity and the two angles of orientation versus spin axis. Using n times 6 equations for n different field conditions (variable in field direction and amplitude) these 8 elements can simply be determined by minimizing the spin tone frequencies in the field magnitude.

The remaining four elements—spin axis offset and scale value, scale value of spin plane components and spin phase—have to be determined by criteria derived from field properties (e.g. non compressible waves) and field models (e.g. IGRF). Special field conditions are required for this calibration. The determination of sensitivities and spin phase need the Earth fields which is known by models at the perigee at least with an accuracy of 0.1%. The spin axis offsets can be determined during solar wind passages in the first summer season and later more rarely at low field in the magnetosphere at selected intervals. Additionally the comparison of magnetic field measurements between the spacecraft can be used for calibration. At special field conditions it can be assumed that the field is homogeneous over the distance of the probes ($\mathbf{B}_1 = \mathbf{B}_n$), spatially linearly distributed and current free ($\operatorname{curl}\mathbf{B} = 0$), or only spatially linearly distributed ($\operatorname{div}\mathbf{B} = 0$). Themis constellations which fulfill these requirements are rare and, if available, e.g. in solar wind, the spin axis offsets can also be determined by single spacecraft analysis. Therefore the spacecraft comparison might be useful to check the in-flight calibration from time to time but cannot provide a significant input for the routine in-flight calibration. As described above, different field conditions are necessary for one in-flight calibration. It has to be assumed that the elements are constant over the whole calibration interval. Therefore the repeatability of the in-flight calibration (at least once per orbit) defines the requirements on the stability of the magnetometer. On the other hand the results of the in-flight calibration present a reality check of the instrument stability.

Calibration results are available for the first half a year of FGM operations. All angles and scale values were constant with an accuracy of 10^{-4}.

Figure 21 shows the offset behavior of the spin plane components of spacecraft A. Both offsets vary less than 0.2 nT over half a year.

In Fig. 22 the standard deviation of all offsets within this interval is plotted. The maximum variation is less than 0.3 nT/6 month. The required stability was 0.2 nT/12 hours.

The statistics has been done for spin-plane offsets only. Spin plane offsets are easy to determine, since the offset is a DC contribution to a signal that should have a spin-frequency variation. The few spin axis offsets we got from solar wind passages are variable in the same order of magnitude, so that we can assume that the stability presented for spin plane offsets is representative for all axes.

To consider the time dependency of the calibration parameters, CalFiles are updated each day, which is the orbital period of the inner spacecraft. Additionally high resolution

Fig. 21 Offset of Probe A spin plane components in the first half year of flight

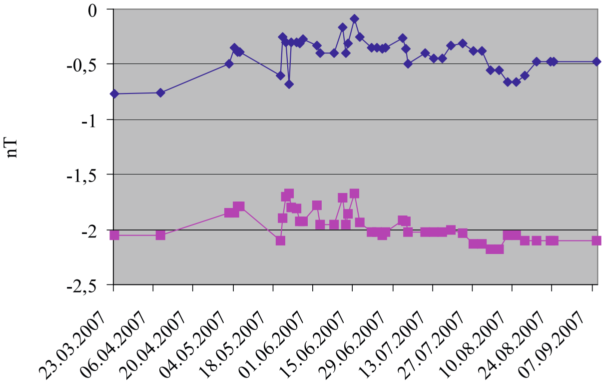

Fig. 22 Offset variation (standard deviation in nT) of spin plane components of all five Probes

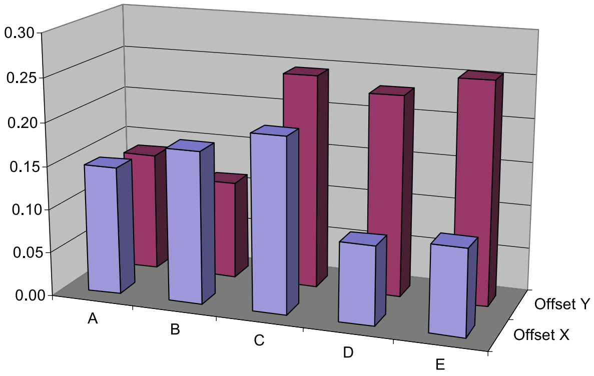

CalFiles can be provided on request. These files are based on daily CalFiles with small adaptations of the two spin plane offsets, one scale value and the angle between the two spin plan components. This is not a calibration in the truest sense of the word, because in an underdetermined system simply the most prominent 4 elements are modified in order to minimize the spin tones in the field magnitude.

5.2 Spacecraft Interferences

Two types of interferences could be detected in space. Both have maximum amplitude of 0.3 nT peak to peak. The first one is related to the solar cells driven power management and therefore strongly spin synchronized. A model of this interference has been developed. After the spin axis was aligned precisely at high field conditions, the remaining content of spin frequency and its harmonics of the spin axis component at low field conditions has been used as input parameter for the model. The derived field wavelet was scaled for the spin plane components by the amplitude of the spin tone harmonics and subtracted from the raw data. Figure 23 shows the dynamic spectra of the spin axis component in SSL system before and after correction. The error in spin tone of 35 pT and double spin tone of 15 pT could be suppressed by a factor of four. The remaining periodic content of spin tone appearing in the corrected data can be interpreted as a non constant phase of the interference with respect to the sun pulse. This seems reasonable because the sun dependent power switch sequence is synchronized with a finite time resolution.

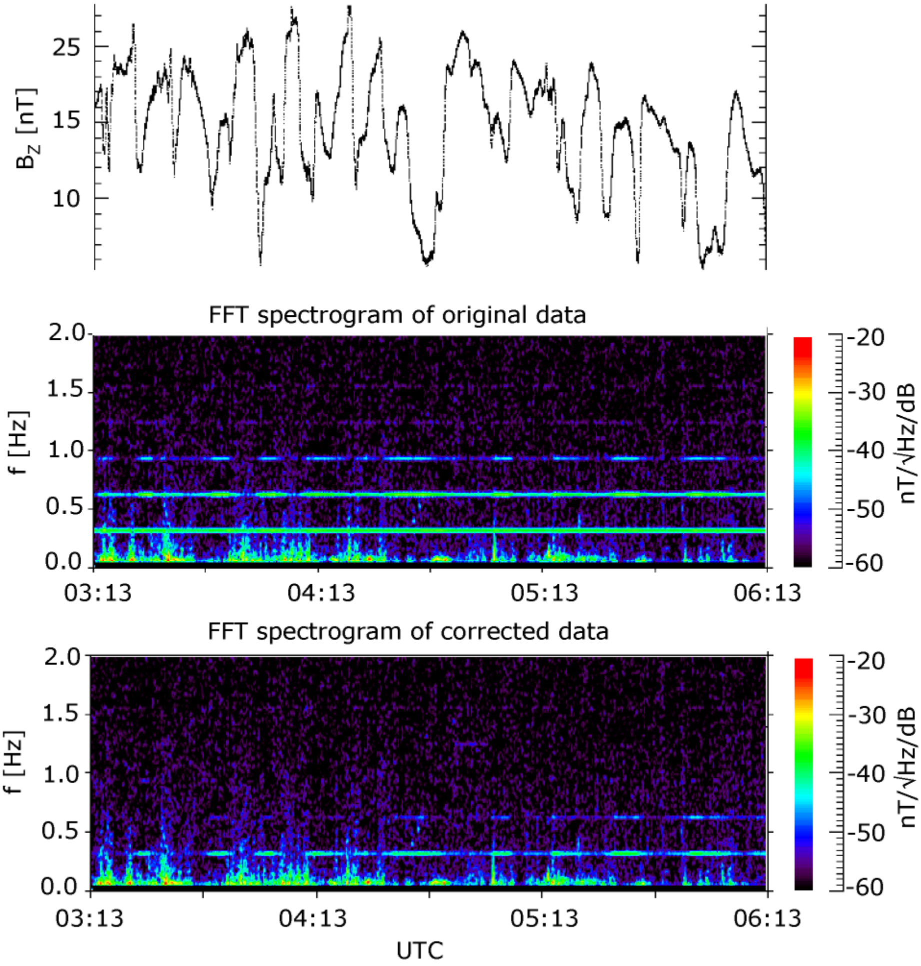

Fig. 23 Data before and after correction of interferences induced by the power supply. *Upper panel*: time plot of the spin axis component. *Central panel*: dynamic spectra of original spin axis data. *Bottom panel*: dynamic spectra of spin axis data after applying the correction using the sun pulse triggered interference model. The FFTs are calculated using 128 4 Hz samples

The second error is caused by sectoring of the particle instruments. The signatures measured by the magnetometer are certainly not generated by mode dependent magnetic moments of the particle instruments. The interference is conducted due to the power profile of the particle instruments. Facilities to detect the interferences in the magnetic field data (see Sect. 4.4) as well as grounding options to prevent the magnetic field measurement from conducted interferences were available. Due to the complex test assembly for such a test on bench level (sun simulation & operation of more than one experiment) the common operation has unfortunately never been tested on ground. The sectors are switched by the 32nd part of a spin period. This corresponds to a 11 Hz switch frequency. Also the sector switching is performed by a finite time resolution continuously synchronized by the sun pulse. This leads to a jitter in the switch frequency and therefore to a dilatation of the interference frequencies. The disturbance can be avoided by changing the flight software timing. It will

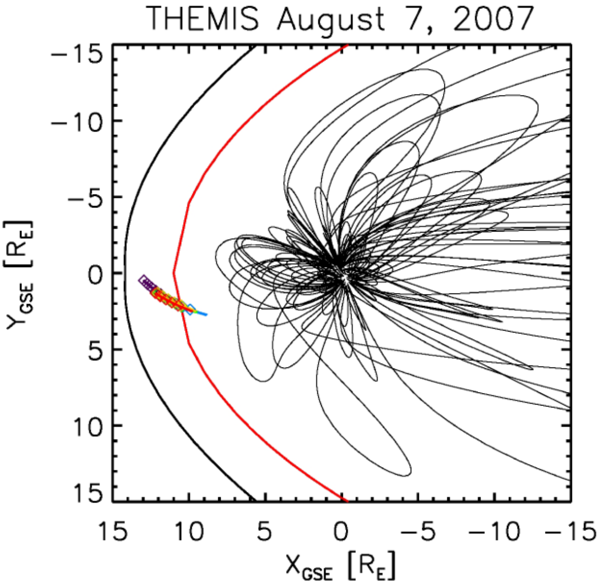

Fig. 24 Themis orbits on August 7 2007 between 09:00 and 11:30 UT. The magnetic field has been obtained using the Tsyganenko 96 model

be done only in a later phase of the mission because the amplitude of the interference is small (0.1 nT) and the affected frequency bands ($n \times 11$ Hz $\pm$ 2 Hz) are covered by SCM (Roux et al. 2008) too.

5.3 Magneto Pause (MP) Oscillations Visible in FGM Data

To demonstrate the FGM capabilities we study a magnetopause crossing which occurred on August 7, 2007 close to the sub-solar point. At this date, the spacecraft were still in the injection phase, sharing the same orbit with a 15.4 RE apogee (see Fig. 24). This "string of pearls" configuration is particularly well suited for timing analysis of the magnetopause position.

Figure 25 shows the magnetic field magnitude measured by all five probes between 09:00 and 11:30 UT as they move from the magnetosheath into the magnetosphere. Probe A, being the last in the string, does not reach the magnetopause during this time interval. The first to cross the magnetopause is probe B at around 09:25 UT. Probes C, D, and E follow five minutes later, one shortly after another. During the following 90 minutes all four leading probes experience multiple magnetopause crossings. Due to the fact that the spacecraft move along the same track we can draw a position-time diagram such as the one shown in Fig. 26. Here we plotted the distance along the orbit, from a common reference point to each spacecraft as a function of time. It can be seen that probe B leads the formation, at a distance of about 1 R_E from probes C, D, and E, which are grouped closer together. About 1.5 R_E away, Probe A closes the formation. A magnetopause crossing detected at a certain moment in time by one of the spacecraft is represented by a dot on the corresponding line.

From the slope of each crossing we can derive the speed of the magnetopause along the spacecraft orbit. The resulting mean values are 72 km/s for inward motion and −95 km/s for outward motion. These values are comparable with 67 km/s, which is the maximum speed of the magnetopause motion if we assume harmonic oscillations.

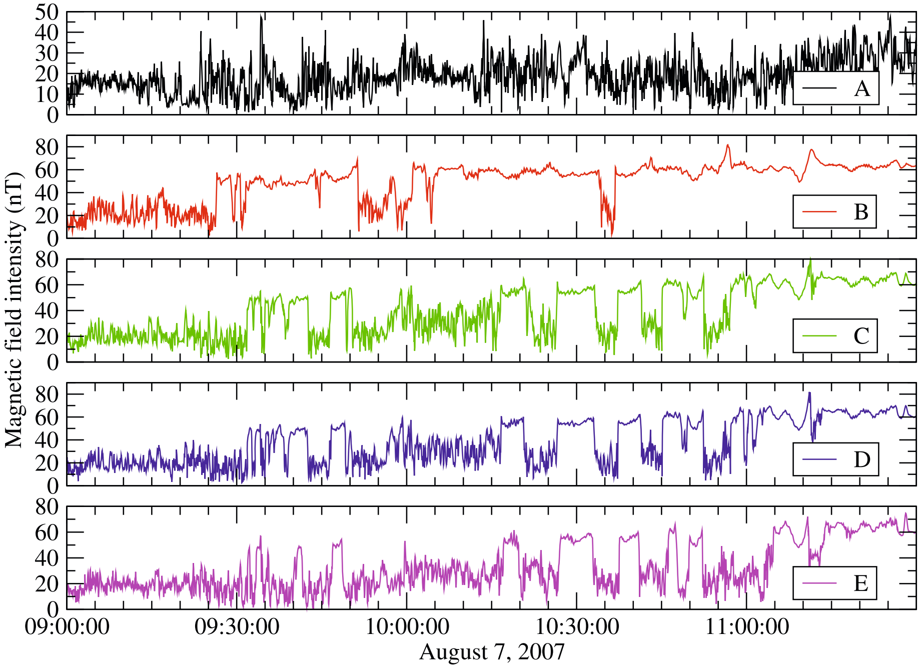

Fig. 25 The magnetic field magnitude measured by Themis magnetometers. All probes but Themis A exhibit multiple magnetopause crossings

In total we detect 81 single-spacecraft events which group themselves in 17 crossings. The motion of the magnetopause is visible in the position-time diagram as indicated by the curved line connecting the crossings between 10:10 and 11:00 UT. Roughly, we see an oscillation with an amplitude of about 2 R_E and a period close to 10 minutes.

6 Summary

The THEMIS FGM benefits from elaborate works for the development of ring cores and the sensor design, the technology of digital fluxgate magnetometers, and tests and calibrations in the high precision facilities developed for a number of previous missions. The general characteristics of FGM, calibration procedure and results are summarized in the present paper.

FGM provides accurate and stable magnetic field measurements in the near-Earth space. The stability was proven to be better than 0.5 nT during the first half year operation. Five point measurements lead to a number of data analysis methods. One example is presented from the magnetopause crossings and the speed of the magnetopause motion is estimated. This reconstruction of the time history of the magnetopause motion is a good example of a new analysis method which uses the specific Themis multi-point configuration.

Acknowledgement The THEMIS team is greatly indebted to many individuals who made the THEMIS mission possible and who contributed greatly to the success of developing, building, testing, and flying the FGM instrument. Special thanks are to Ernst Jelting and Sabine Filbrandt (IGEP Braunschweig) for carefully

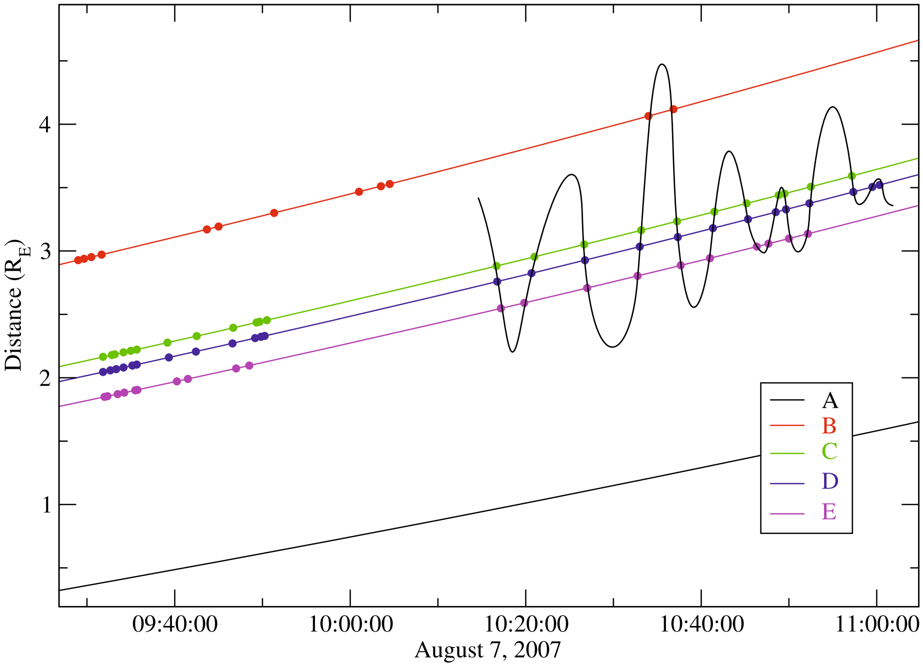

Fig. 26 Position-time diagram of the magnetopause crossings. The y-axis shows the distance along the orbit. For each spacecraft there is a position curve on which the magnetopause crossings are marked

handling the many technical and financial activities of the Lead Investigator group in Braunschweig. The Project Team at UCB has done an outstanding job in running the THEMIS project. Special thanks go to Peter Harvey, Vassilis Angelopolous, and Dave Sibeck. Financial support for the work of the FGM Lead Investigator Team at the Technical University of Braunschweig by the German Ministerium für Wirtschaft und Technologie and the Deutsches Zentrum für Luft- und Raumfahrt under grant 50QP0402 is acknowledged. Financial support of the Austrian Academy is also gratefully acknowledged. THEMIS was made possible by NASA, under contract NAS5-02099.

References

V. Angelopoulos, The Themis Mission, Space Sci. Rev. (2008, this issue). doi:10.1007/s11214-008-9336-1

H.U. Auster, A. Lichopoj, J. Rustenbach, H. Bitterlich, K.H. Fornacon, O. Hillenmaier, R. Krause, H.J. Schenk, V. Auster, Meas. Sci. Technol. **6**, 477–481 (1995). doi:10.1088/0957-0233/6/5/007

H.U. Auster, K.H. Fornacon, E. Georgescu, K.H. Glassmeier, U. Motschmann, Meas. Sci. Technol. **13**, 1124–1131 (2002). doi:10.1088/0957-0233/13/7/321

H.U. Auster, I. Apathy, G. Berghofer, A. Remizov, R. Roll, K.H. Fornacon, K.H. Glassmeier, G. Haerendel, I. Hejja, E. Kührt, W. Magnes, D. Moehlmann, U. Motschmann, I. Richter, H. Rosenbauer, C.T. Russell, J. Rustenbach, K. Sauer, K. Schwingenschuh, I. Szemerey, R. Waesch, Space Sci. Rev. **128**, 221–240 (2007). doi:10.1007/s11214-006-9033-x

A. Balogh, C.M. Carr, M.H. Acuna, M.W. Dunlop, T.J. Beek, P. Brown, K.-H. Fornacon, E. Georgescu, K.H. Glassmeier, J. Harris, G. Musmann, T. Oddy, K. Schwingenschuh, Ann. Geophys. **19**, 1207–1217 (2001)

W. Baumjohann, G. Haerendel, R.A. Treumann, T.M. Bauer, J. Rustenbach, E. Georgescu, U. Auster, K.H. Fornacon, K.H. Glassmeier, H. Lühr, J. Büchner, B. Nikutowski, A. Balogh, S.W.H. Cowley, Adv. Space Res. **24**, 77–80 (1999). doi:10.1016/S0273-1177(99)00428-7

C. Carr, P. Brown, T.L. Zhang, J. Gloag, T. Horbury, E. Lucek, W. Magnes, H. O'Brien, T. Oddy, H.U. Auster, P. Austin, O. Aydogar, A. Balogh, W. Baumjohann, T. Beek, H. Eichelberger, K.H. Fornacon, E. Georgescu, K.H. Glassmeier, M. Ludlam, R. Nakamura, I. Richter, Ann. Geophys. **23**, 2713–2732 (2005)

M.K. Dougherty, S. Kellock, D.J. Southwood, A. Balogh, E.J. Smith, B.T. Tsurutani, B. Gerlach, K.H. Glassmeier, F. Gliem, C.T.G. Erdos, F.M. Neubauer, S.W.H. Cowley, Space Sci. Rev. **114**, 331–383 (2004). doi:10.1007/s11214-004-1432-2

K.H. Fornacon, H.U. Auster, E. Georgescu, K.H. Glassmeier, G. Haerendel, J. Rustenbach, M. Dunlop, Ann. Geophys. **17**, 1521–1527 (1999). doi:10.1007/s00585-999-1521-3

K.H. Glassmeier, U. Motschmann, M. Dunlop, A. Balogh, M.H. Acuna, C. Carr, G. Musmann, K.H. Fornacon, K. Scheda, J. Vogt, E. Georgescu, S.J. Buchert, Ann. Geophys. **19**, 1439–1448 (2001)

K.H. Glassmeier, I. Richter, A. Diedrich, G. Musmann, U. Auster, U. Motschmann, A. Balogh, C. Carr, E. Cupido, A. Coates, M. Rother, K. Schwingenschuh, K. Szegö, B. Tsurutani, Space Sci. Rev. **128**, 649–670 (2007a). doi:10.1007/s11214-006-9114-x

K.H. Glassmeier, H. Boehnhardt, D. Koschny, E. Kührt, I. Richter, Space Sci. Rev. **128**, 1–21 (2007b)

P. Harvey, E. Taylor, R. Sterling, M. Cully, Space Sci. Rev. (2008, this issue)

M. Ludlam, V. Angelopoulos, E. Taylor, R.C. Snare, J.D. Means, Y. Ge, P. Narvaez, H.U. Auster, O. LeContel, D. Larson, T. Moreau, Space Sci. Rev. (2008, this issue)

M. Müller, T. Lederer, K.-H. Fornacon, R. Schäfer, J. Magn. Magn. Math. **177**, 231–232 (1998)

A. Roux, O. Le Contel, P. Robert, C. Coillot, A. Bouabdellah, B. la Porte, D. Alison, S. Ruocco, M.C. Vassal, Space Sci. Rev. (2008, this issue)

L. Zanetti, T. Potemra, R. Erlandson, Space Sci. Rev. **70**, 465–482 (1994). doi:10.1007/BF00756882

T.L. Zhang, W. Baumjohann, M. Delva, H.U. Auster, A. Balogh, C.T. Russell, S. Barabash, M. Balikhin, G. Berghofer, H.K. Biernat, H. Lammer, H.I.M. Lichtenegger, W. Magnes, R. Nakamura, T. Penz, K. Schwingenschuh, Z. Vörös, W. Zambelli, K.H. Fornacon, K.H. Glassmeier, I. Richter, C. Carr, K. Kudela, J.K. Shi, H. Zhao, U. Motschmann, J.-P. Lebreton, Planet. Space Sci. **54**, 1336–1343 (2006). doi:10.1016/j.pss.2006.04.018